Available online at www.sciencedirect.com
ScienceDirect
Trans. Nonferrous Met. Soc. China 34(2024) 4032−4048
Transactions of Nonferrous Metals Society of China
www.tnmsc.cn

Influence of axial stress on failure characteristics of deep arched hard rock roadway

Kang PENG, Ren-zhi LAI, Song LUO, Xi-bing LI

School of Resources and Safety Engineering, Central South University, Changsha 410083, China

Received 10 May 2023; accepted 21 December 2023

Abstract: To study the influence of axial stress on the failure characteristics of deep arched roadway considering structural effect, true triaxial compression tests were conducted on cubic granite specimens with a three-centered arched hole structure. A video monitoring device was utilized to record the failure process of surrounding rocks. The test results show that under 10−60 MPa axial stress, the surrounding rock failure process included the calm stage, particle ejection stage, fragment ejection stage, and rock slice buckling and spalling stage. Under higher axial stresses (70 and 80 MPa), the failure process is characterized by violent fragment spray during the fourth stage. As the axial stress increases, the failure of surrounding rock increases, while the initial vertical failure stress first increases and then decreases. According to the failure characteristics of roadway under different axial stresses, arranging the roadway along the direction of a moderate axial stress level is desired.

Key words: axial stress; failure characteristic; true triaxial test; arched roadway; V-shaped notch; acoustic emission; rockburst

1 Introduction

Rockburst is a sudden rock failure phenomenon caused by deep underground excavation, often accompanied by varying degrees of sound and energy release [1−3]. As underground space projects have progressed to increasing depths, the stability of rock mass has been significantly affected by “high ground stress, high permeability, high ground temperature and strong mining disturbance” [4−6]. The stress environment becomes increasingly complex, and rockburst disasters occur occasionally [7,8]. This sudden geological hazard poses a major threat to the safety of personnel and equipment [9,10].

Many researchers have studied the mechanism and failure characteristics of rockburst. In the early stages of rockburst study, laboratory tests were mainly performed to investigate pillar and excavation boundary rockbursts. The uniaxial compression tests [11,12] and biaxial compression tests [13−15] were the most prevalent types of tests. Later, with the emergence of true triaxial equipment, researchers preferred to conduct true triaxial experiments for more realistic stress conditions, and intact rectangular prismatic or cubic rock specimens were normally used to study rockburst issues [16,17]. LI et al [18,19] conducted true triaxial unloading tests on different cuboidal rocks (granite, sandstone, and cement mortar) and found that the intermediate principal stress affected the failure mode, peak strength, and rockburst severity of hard rock. SU et al [20] investigated the influence of tunnel axial stress on strainburst using a true triaxial rockburst system. They found that the rock strength first increased and then decreased with increasing axial stress. JIANG et al [21] analyzed

Corresponding author: Song LUO, Tel: +86-13142001519, E-mail: luosong@csu.edu.cn
DOI: 10.1016/S1003-6326(24)66656-2

the strainburst behavior of rectangular prismatic marble specimens under different stress conditions and found that the intermediate principal stress considerably influenced the rockburst behavior.

The above studies have greatly enriched the understanding of rockburst. However, these studies only considered rectangular prismatic rock specimens in the rockburst experiments, and ignored the influence of the whole structure of the chamber or roadway. Thus, they can only simulate the local failure of a roadway, which can not sufficiently reflect the characteristics of roadway rockburst occurring in engineering practice. This is because the structural effect and curvature of the rock mass have an important influence on its mechanical properties in deep subsurface engineering [22]. For this reason, researchers have attempted to carry out rockburst simulation experiments considering the whole rock structures [23−25]. WANG et al [26] used a self-developed true triaxial test system to carry out rockburst simulation tests on square specimens with elliptical holes, and studied the influence of the long-short axis ratio on rockburst of an elliptical tunnel structure. HU et al [27] studied the rockburst process of a borehole by using a cubic specimen with prefabricated circular holes. Their test results showed that the rockburst process was characterized by significant spatial distribution and structural responses. YANG et al [28] investigated the effect of horizontal stress on the rockburst proneness of different rocks using a digital drilling instrument. GONG et al [29] and SI et al [30,31] also performed a series of true triaxial tests on cubic specimens with prefabricated holes and obtained important results. However, these existing studies overlook the influence of axial stress on the failure characteristics of roadway structures. In addition, at the excavation boundary, the rock is often subjected to a special stress state of "one face free, five faces under stress". In this stress state, in addition to the tangential and radial stresses, the axial stress of the chamber influences rock failure [20]. Unfortunately, the boundary effect on the failure characteristics of the surrounding rock in a deep arched roadway has rarely been investigated by comparative experiments considering the influence of axial stress.

In deep underground engineering, the most common and representative cross-sectional shape is the three-centered arch [32]. Therefore, in this study, groups of true triaxial compression tests were conducted under different axial stress levels using cubic granite specimens with a three-centered arched hole. A self-developed video device was used to record the failure process and characteristics of surrounding rock. The test process and results were analyzed in detail with acoustic emission (AE) signals. Moreover, comparative tests were also conducted using the rock specimens with a smaller hole size to discuss the boundary effects on the failure characteristics of surrounding rock in deep roadways. The results of this study can help guide the excavation and support of deep roadways.

2 Experimental

2.1 Preparation of samples

The granite material in this study was obtained from Wushan Town, Suizhou City, Hubei Province, China. The material's uniaxial compressive strength, elastic modulus, Poisson's ratio, density, and P-wave velocity were 145 MPa, 31.78 GPa, 0.24, 2620 kg/m^3, and 2923 m/s, respectively. The granite was judged to have a strong rockburst tendency using the potential energy of elastic strain index [33,34]. Additionally, an X-ray diffraction (XRD) experiment was conducted on the granite material to analyze its diffraction patterns. The mineral composition of the granite is shown in Fig. 1(a). The granite used in the experiment mainly consists of albite, quartz, microcline, anorthite, orthoclase, sanidine and biotite. The detailed mineral proportions are shown in Fig. 1(b).

To reduce the discreteness of rock specimens and to ensure testing accuracy, all specimens were taken from the same intact rock block. As shown in Fig. 2, the granite block was machined into cubic specimens with side lengths of 100 mm, and an arched penetration hole (with bottom hole length of 50 mm, sidewall height of 25 mm, and arch height of 16.67 mm) was drilled in the center of the specimens. These cubic granite specimens were machined with strict accuracy according to the standards of the International Society for Rock Mechanics [35].

2.2 Test equipment

The cubic granite specimens were tested using a true triaxial testing system, as shown in Figs. 3(a)

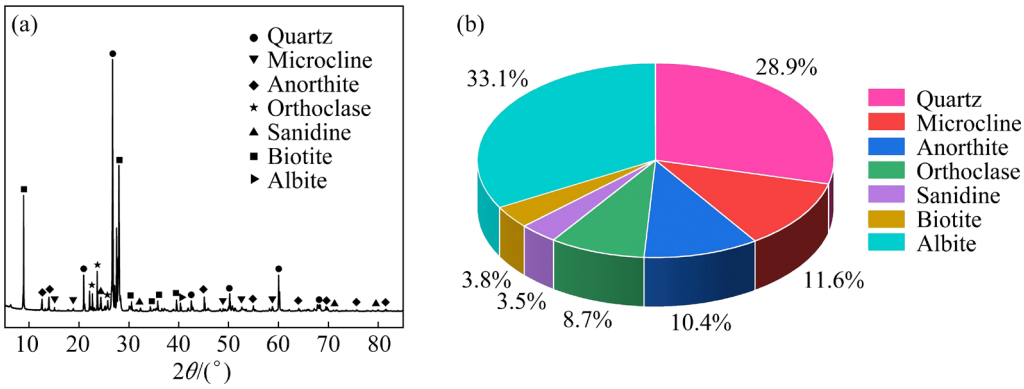

Fig. 1 X-ray diffraction pattern (a) and mineral composition (b) of test material

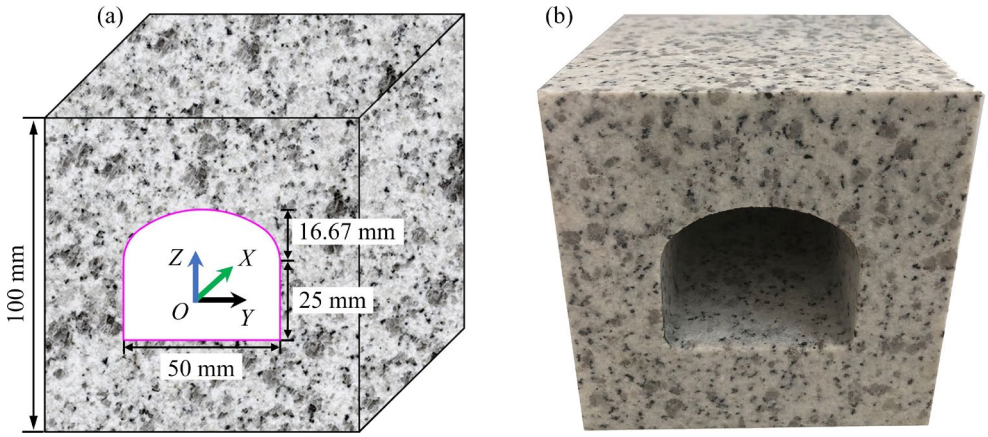

Fig. 2 Prepared granite specimen: (a) Sketch; (b) Physical photograph

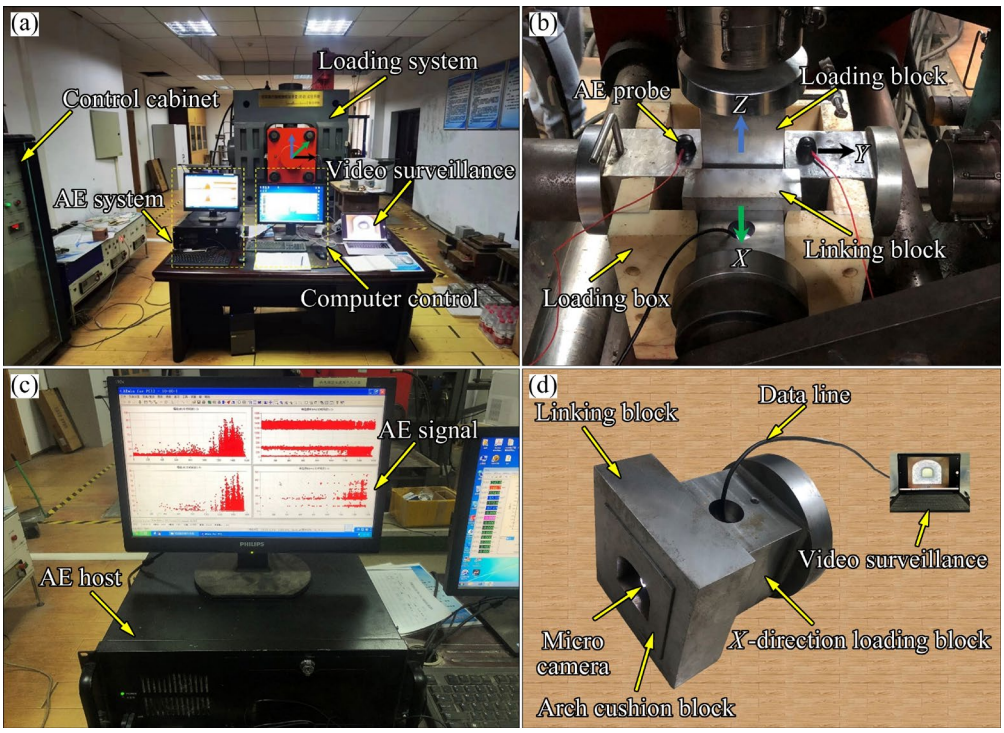

Fig. 3 Test equipment: (a) True triaxial test system; (b) True triaxial loading box; (c) PCI−2 AE system; (d) Video monitoring device

and (b). The test system can apply loads independently in the X, Y, and Z directions. The maximum load that can be applied in X and Y directions is 2 MN, and that in the Z direction is 3 MN. The load rate range is 10^1−10^4 N/s. The force, displacement, deformation, and other information are recorded in real-time using a full digital measurement and control device, which can realize one-way, two-way, and three-way instantaneous loading and unloading. The tests were conducted using a PCI−2 AE system (Fig. 3(c)) to monitor the AE signals generated during the tests. A video monitoring device (Fig. 3(d)) was developed, with a miniature camera placed in a special X-directional loading block to observe the whole process of failure development in the inner wall of the hole in real-time. A three-centered arch block of the same size as the specimen hole was added to ensure full contact of the loading block with the specimen containing the hole. The block and loading block were connected using a linking block.

2.3 Load path

Following excavation of the working face, stress concentration will gradually occur at the boundary, and the tangential stress σ_θ will continue to increase. When σ_θ increases beyond the rock strength, the rock will rupture and the residual strain energy will be rapidly released in the form of a rockburst. During this stress adjustment process, the rock at the excavation boundary is also subjected to the radial stress σ_y and axial stress σ_x, with $\sigma_\theta > \sigma_x > \sigma_y$ [20]. In indoor laboratory experiments, an increase in σ_θ can be simulated by increasing the vertical stress σ_z [27]. Therefore, in this study, σ_y was set at 10 MPa, σ_x was set at eight stress levels from 10 to 80 MPa, in increments of 10 MPa. By increasing σ_z to simulate an increase in σ_θ in the chamber, the influence of σ_x on the failure characteristics of the arched roadway was systematically studied.

The specific load path is shown in Fig. 4. In the present experiments, the axial and radial directions of the hole are the X- and Y-direction, respectively. After installing the granite specimen in the loading box, force-controlled loading was applied in all three directions at 1 kN/s. First, σ_x, σ_y, and σ_z were loaded to 10 MPa and kept in a hydrostatic pressure state for 2 min. Then, σ_x and σ_z were loaded to the set axial stress value, and the hydrostatic pressure state was maintained for 2 min. Subsequently, we continued to load σ_z. To allow the surrounding rock to adjust to the stress and fully observe the whole failure process, the continuous loading in Z-direction is gradually switched to step loading (20 kN per step and maintained for 1 min) as the cavern wall exerts particle ejection. When the applied load causes wall failure in the entire axial direction or severely damages both sides of the wall, step loading is stopped, maintained for 60 s, and finally the force in the three directions is released simultaneously in a 20 mm/min displacement control mode.

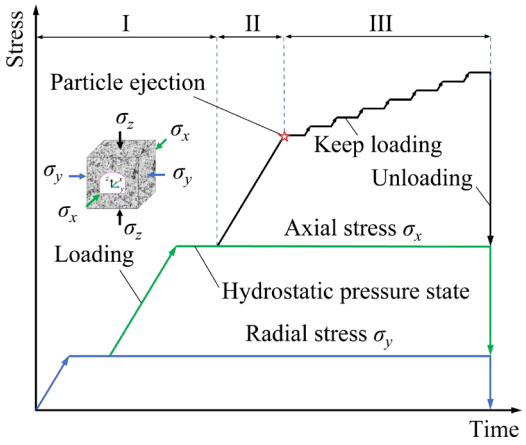

Fig. 4 Test load path: Initial loading (I); Continuous loading (II); Step loading (III)

3 Experimental results

3.1 Stress–time curves

The stress–time curves for the true triaxial test under different axial stress conditions are shown in Fig. 5. The samples are named as follows: For example, in Specimen T-10-50, T represents the triaxial compression test, and 10 and 50 represent the radial and axial stress setting values, respectively. Because of the hole in the X-direction, the contact area of the specimen in the X-direction is smaller than that in the Y- and Z-direction. Hence, the load rate and stress value in the X-direction were converted. The Z-direction stress values at the beginning of failure (particle ejection) in the hole wall under different axial stress conditions were 52.50 MPa (T-10-10), 60.51 MPa (T-10-20), 65 MPa (T-10-30), 77.01 MPa (T-10-40), 79.46 MPa (T-10-50), 89.90 MPa (T-10-60), 79.71 MPa (T-10-70), and 74.29 MPa (T-10-80). The

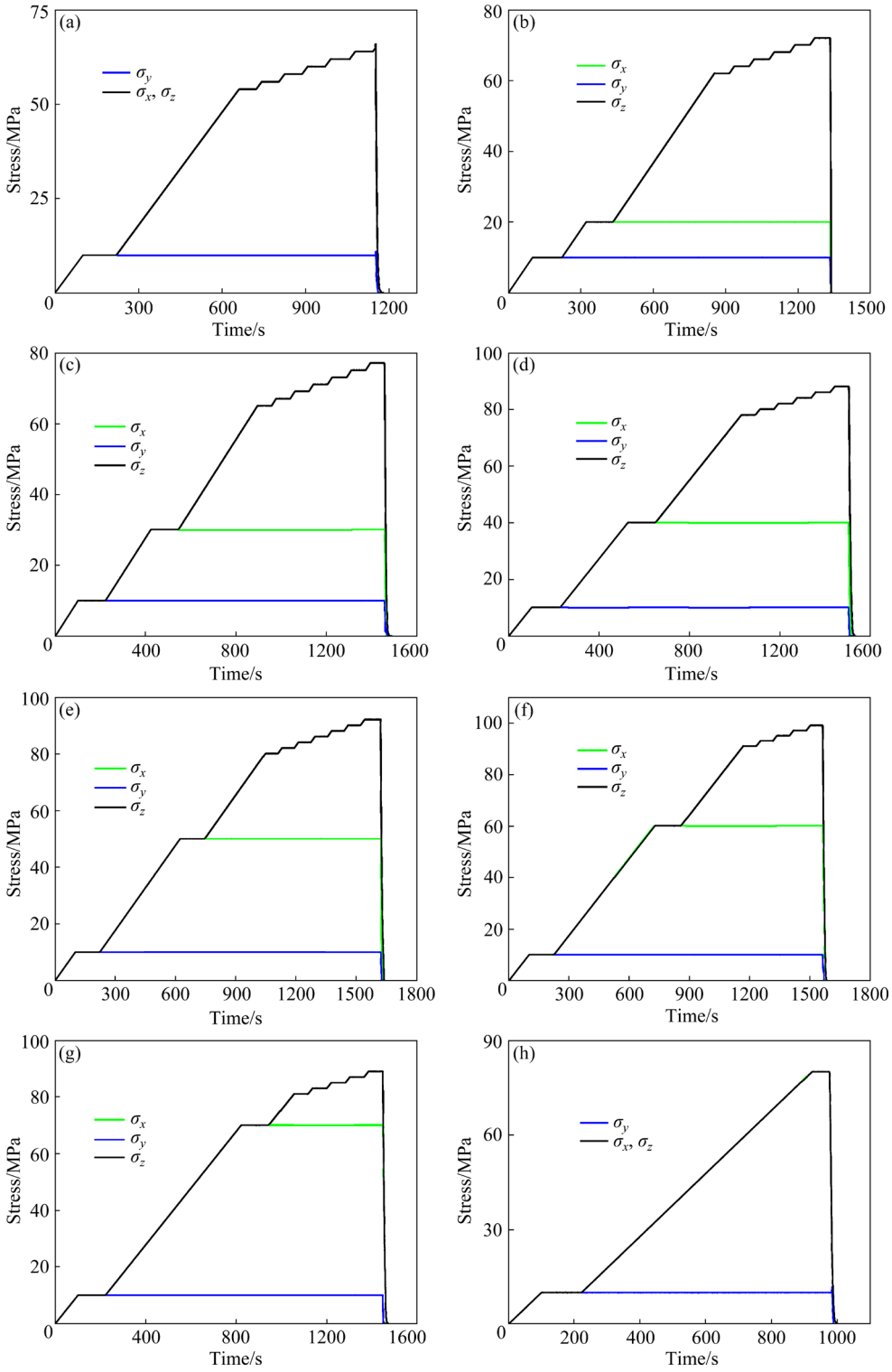

Fig. 5 Stress–time curves of specimens under different axial stress conditions: (a) T-10-10; (b) T-10-20; (c) T-10-30; (d) T-10-40; (e) T-10-50; (f) T-10-60; (g) T-10-70; (h) T-10-80

maximum stress values before final releasing the stress in the Z-direction under different axial stress conditions were 66 MPa (T-10-10), 72 MPa (T-10-20), 77 MPa (T-10-30), 88 MPa (T-10-40), 92 MPa (T-10-50), 99 MPa (T-10-60), 89 MPa (T-10-70), and 80 MPa (T-10-80). In Specimen T-10-80, particle ejection occurred before it was loaded to the set axial stress value. Moreover, axial penetration failure occurred when the specimen was loaded to 80 MPa, and no step loading was performed.

3.2 Failure process of surrounding rock

During the tests, the video monitoring device was used to record the failure process of the rock surrounding the hole. The comparative analysis revealed that at lower axial stresses (10−60 MPa), the failure process of the surrounding rock could be roughly divided into four stages: the calm stage, the particle ejection stage, the fragment ejection stage, and the rock slice buckling and spalling stage. However, at higher axial stresses (70−80 MPa), the failure process was intenser and went through four stages: the calm stage, the particle ejection stage, the fragment ejection stage, and the fragment spraying stage. Taking Specimens T-10-30 (representing low axial stress levels) and T-10-70 (representing high axial stress levels) as examples, the failure process of the surrounding rock is explained in detail to understand the characteristics of each stage further.

The failure process of the surrounding rock of Specimen T-10-30 is shown in Fig. 6. During the calm stage, the surrounding rock does not fail (Fig. 6(a)). At 917.28 s and σ_z=65 MPa, small particles are ejected from the bottom of the right sidewall (Fig. 6(b)). After 68.04 s, σ_z increases to 67.00 MPa, and particle ejection also occurs on the left sidewall (Fig. 6(c)). For the next 138.96 s, particles are continuously ejected from both sidewalls. At 1124.28 s and σ_z=69.20 MPa, the rock block of the right sidewall bottom is suddenly peeled off and ejected (Fig. 6(d)). After 48.24 s, σ_z increases to 71.00 MPa, and fragment ejection accompanied by a large ejection of small particles occurs near the bottom of the right sidewall (Fig. 6(e)), producing a small amount of white dust fog, forming macroscopic cracks. At 1205.64 s, the right sidewall rock slice buckles (Fig. 6(f)). After 39.96 s, σ_z reaches 73.00 MPa, and numerous particles are suddenly ejected from the left sidewall, recreating a white fog phenomenon (lasting for 21.00 s). Simultaneously, the left sidewall rock slice also buckles (Fig. 6(g)). At 1343.52 s and σ_z= 75.00 MPa, small rock slice spalling occurs on the left sidewall, and the crack gradually expands (Fig. 6(h)). After about 3.60 s, the left sidewall rock slice suddenly peels off, and a new rock slice buckling appears on the left sidewall (Fig. 6(i)). Then, the crack gradually expands along the axial direction, with block fragments popping out of the sidewalls on either side. As σ_z gradually increases, the crack on the left sidewall further expands, accompanied by spalling of several block fragments (Fig. 6(j)). When σ_z reaches 75.77 MPa, significant rock slice buckling occurs on the right sidewall (Fig. 6(k)). As σ_z increases further, the right sidewall rock slice continues to buckle and numerous particles ejected from both sidewalls create a small amount of white fog. The final failure

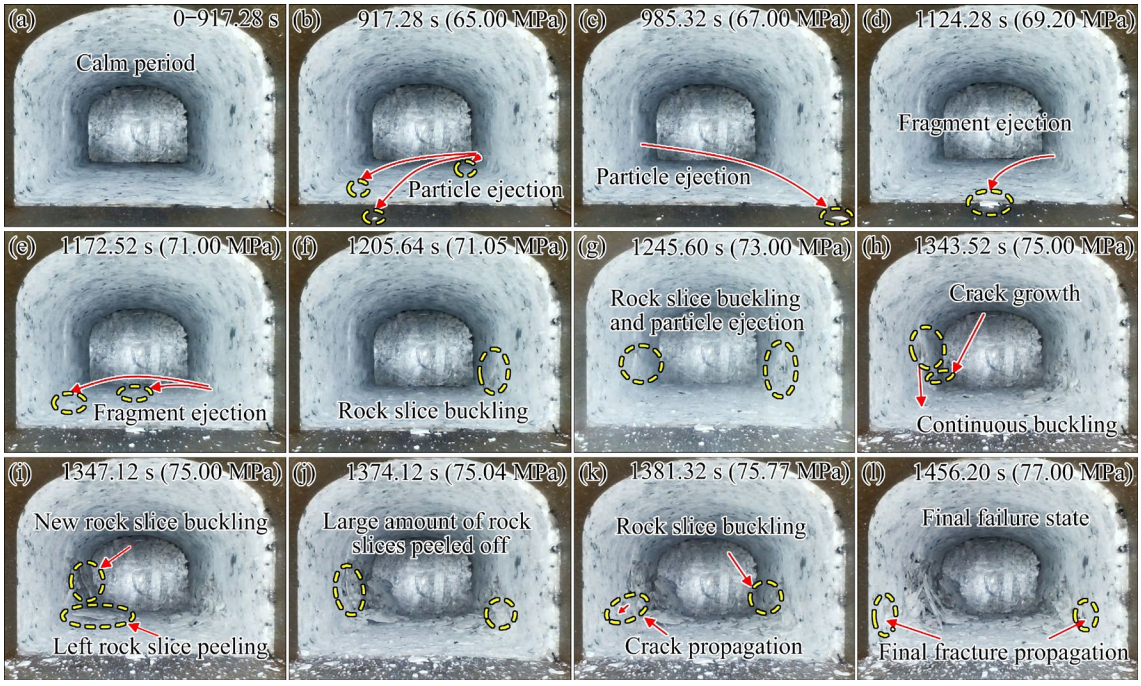

Fig. 6 Failure process images of Specimen T-10-30

state of the surrounding rock is shown in Fig. 6(l). We observed serious failure to both sidewalls, with the failure length reaching more than 3/4 of the hole's axial length.

The failure process of the surrounding rock of Specimen T-10-70 is shown in Fig. 7. During the calm period, the surrounding rock of the hole does not fail (Fig. 7(a)). At 1045.08 s and σ_z=79.71 MPa, particle ejection occurs at the bottom of the right sidewall (Fig. 7(b)). After about 3.96 s, particle ejection reoccurs (Fig. 7(c)). At 1066.32 s, particles are also ejected at the bottom of the left sidewall (Fig. 7(d)). At 1074.24 s and σ_z=81.00 MPa, massive particles are ejected from both sidewalls (Fig. 7(e)). At 1132.20 s and σ_z=82.28 MPa, the fragment ejection distance reached 2/3 of the radial length of the hole following the sudden ejection of fragments from the right sidewall accompanied by a small amount of particle ejection (Fig. 7(f)). At this time, a macroscopic crack appears on the right sidewall. When σ_z increases to 83.00 MPa after 42.12 s, fragment ejection reoccurs on the right sidewall (Fig. 7(g)), and several particles are ejected, creating a white fog phenomenon (lasting for 5 s). At 1206.00 s and σ_z=83.33 MPa, rock slices are suddenly ejected from the left sidewall (Fig. 7(h)). After 22.32 s, the rock slice ejection also occurs at the failure position of the right sidewall (Fig. 7(i)). At 1349.28 s and σ_z=87.00 MPa, several fragments are ejected, producing white fog phenomena; the cracks on both sidewalls gradually develop along the axial direction (Fig. 7(j)). The whole fragment ejection phase lasts for approximately 250 s, with fragments and fine particles being continuously ejected from both sidewalls. At 1383.12 s and σ_z=88.57 MPa, many powdery particles are suddenly ejected from the right sidewall. The spraying of massive rock fragments creates a white fog phenomenon (Fig. 7(k)). The fragment spraying process lasts for 66.60 s. The final failure state of the surrounding rock is shown in Fig. 7(l). Severe failure is observed on both sidewalls of Specimens T-10-30 and T-10-70, indicating the rationality of experimental operation.

3.3 Failure characteristics under different axial stresses

Figure 8 shows the surrounding rock failure after the tests. No failure occurs at the top and bottom of the holes in all specimens. However, there is obvious spalling on the sidewalls. Under low axial stress conditions (Figs. 8(a−f)), the sidewall rock slices are mainly characterized by static slow spalling, generating thin rock slices approximately parallel to the sidewall. In addition, some rock slices are only partially open and not completely peeled off from the sidewall due to incomplete crack development. In contrast, under

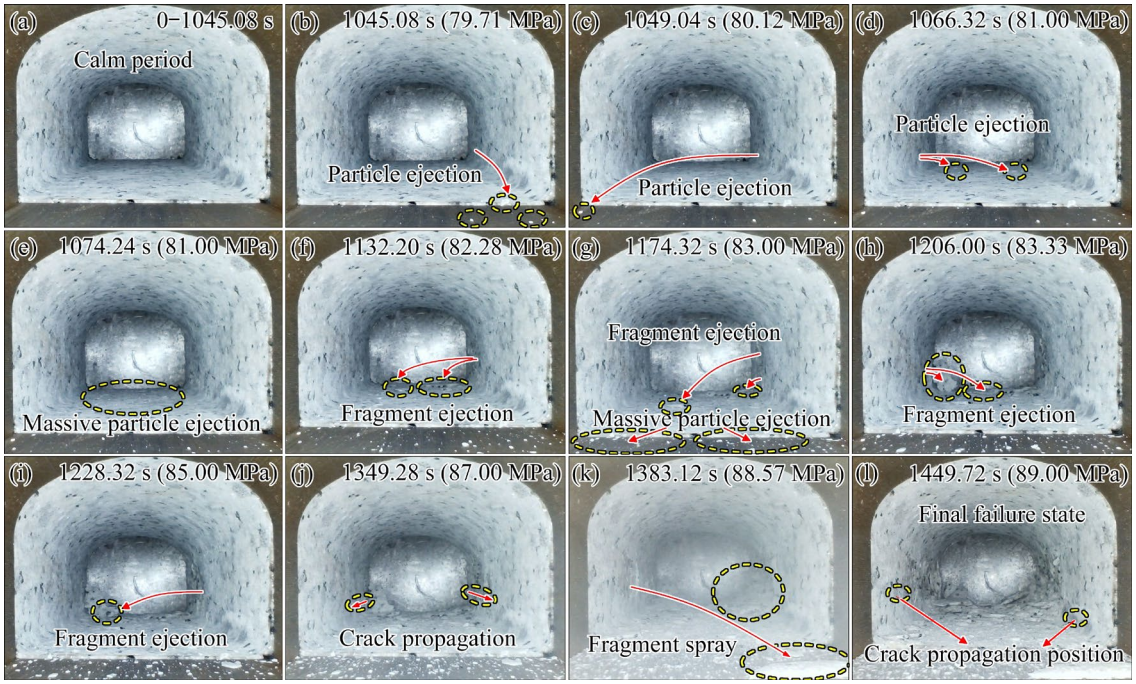

Fig. 7 Failure process images of Specimen T-10-70

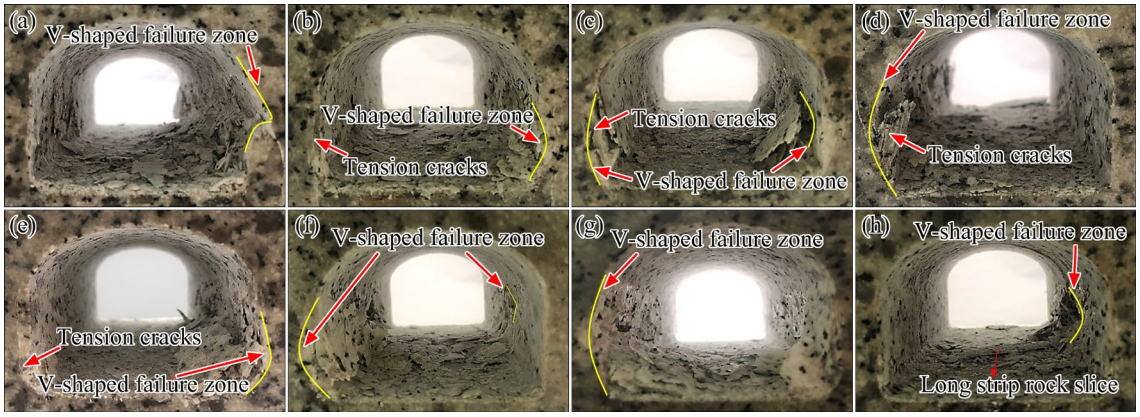

Fig. 8 Failure states of hole sidewalls in rock specimens under different axial stress conditions: (a) T-10-10; (b) T-10-20; (c) T-10-30; (d) T-10-40; (e) T-10-50; (f) T-10-60; (g) T-10-70; (h) T-10-80

high axial stress conditions, the spalling of the surrounding rock on the sidewalls is intenser (as shown in Figs. 8(g) and (h)), with rock slices ejected from one side of the cavern sidewall to the other. Under the influence of rock heterogeneity, the failure degree of both sidewalls is different. However, the failure pattern is V-shaped and is characterized by deep middle and shallow ends in the vertical direction. In Figs. 8(b−e), laminar cracks roughly parallel to the sidewall can be observed at the sidewall boundary, indicating that the spalling of rock slices is due to tensile failure.

When the axial stresses are 10 and 20 MPa, the size of rock slices is significantly smaller than that produced at the axial stress of 30−70 MPa, and such rock slices dominate during the spalling. This is because, under high axial stress, it is relatively difficult to produce tensile stress in the axial direction of the hole due to the clamping of axial stress, and the tensile stress is more limited to the radial direction. Therefore, the crack tends to develop in the vertical and axial directions, producing significantly larger rock slices. However, when the axial stress is too high, the excessive axial stress will moderately inhibit the crack development along the axial direction, promoting their development along the vertical direction. Thus, a long strip of rock slice is produced (see Fig. 8(h)).

3.4 AE characteristics under different axial stresses

The AE activity generated during the true triaxial compression tests can intuitively reflect the evolution of internal cracks in the surrounding rock. Therefore, in this work, two AE probes were mounted on the two load blocks in the *Y*-direction to monitor the AE signals generated during the tests. The characteristics of the AE counts and cumulative AE counts under different axial stress conditions are shown in Fig. 9. Extensive AE activity is produced in Specimen T-10-80 before reaching the initial stress state and much macroscopic failure on the sidewall. Hence, no step loading is performed on this specimen. In Figs. 9(a−g), during the initial and continuous loading phases (see Fig. 4), the primary cracks inside the specimen gradually close under the force, generating a small amount of AE activity. The sudden generation of more AE activity near the start of step loading indicates that internal cracks in the surrounding rock are initiating and expanding. When the cracks extend to the surface of the sidewall, rock particles are ejected under the force. Large amounts of AE activity are generated when the vertical stress is sufficiently high. At this time, internal cracks in the surrounding rock expand, unite, and penetrate until macroscopic failure occurs on the sidewall. In the step-loading stage, the AE signal generated by the crack activity occurs during the stress maintenance period, indicating an effectiveness of the step-loading.

4 Discussion

4.1 Influence of axial stress on failure evolution

Under similar true triaxial compression conditions, the failure evolution of hole sidewalls in the specimens can be different due to a change in axial stress. As demonstrated in Fig. 10, when the axial stress is relatively low (10−60 MPa), the evolution process of the sidewall failure can be divided into four stages: the calm stage, the particle

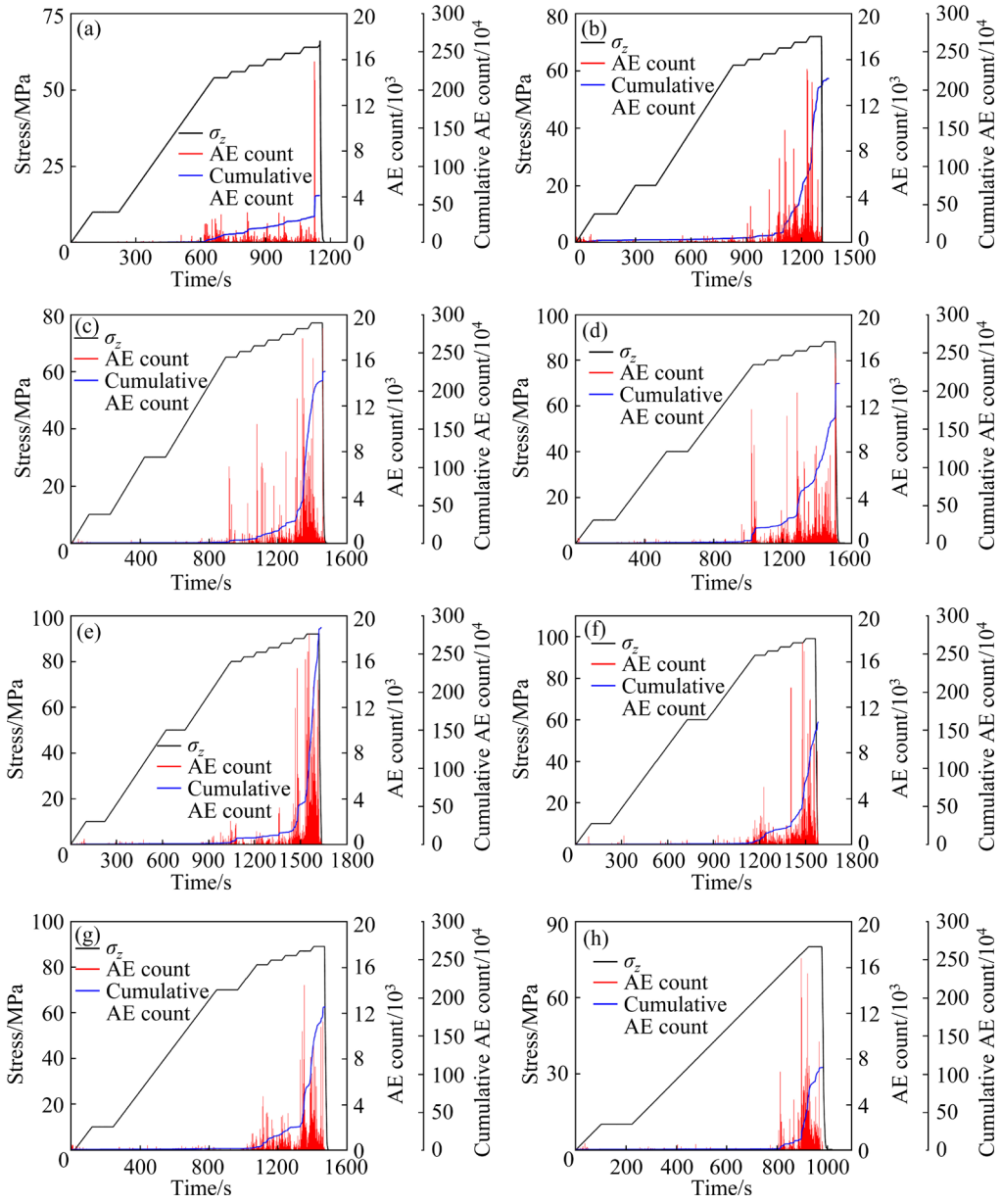

Fig. 9 AE activity characteristics of rock specimens under different axial stress conditions: (a) T-10-10; (b) T-10-20; (c) T-10-30; (d) T-10-40; (e) T-10-50; (f) T-10-60; (g) T-10-70; (h) T-10-80

ejection stage, the fragment ejection stage, and the rock slice buckling and spalling stage. The characteristics of different failure stages under low axial stress conditions are as follows. (1) The calm stage: There is no macroscopic failure to the sidewalls. As the vertical stress gradually increases, the elastic strain energy continuously accumulates and microcracks gradually initiate on the sidewalls. (2) The particle ejection stage: As the cracks gradually expand, rock particles are ejected from the sidewall, and this process occurs mainly at the bottom of the sidewalls. The main reason is that the bottom of the sidewalls is located at the junction of the sidewalls and the bottom plate, which is prone to stress concentration. Therefore, rock failure occurs here first. As the vertical stress increases, particle ejection gradually occurs along the axial direction of the hole. (3) The fragment ejection stage: As the cracks continue to expand, some cracks become interconnected. Rock fragments are produced and ejected from the sidewalls due to the release of the stored elastic strain energy, simultaneously accompanied by particle ejection. At this time, macroscopic cracks are generated on the sidewalls. (4) The rock slice buckling and spalling stage: As the vertical stress continuously

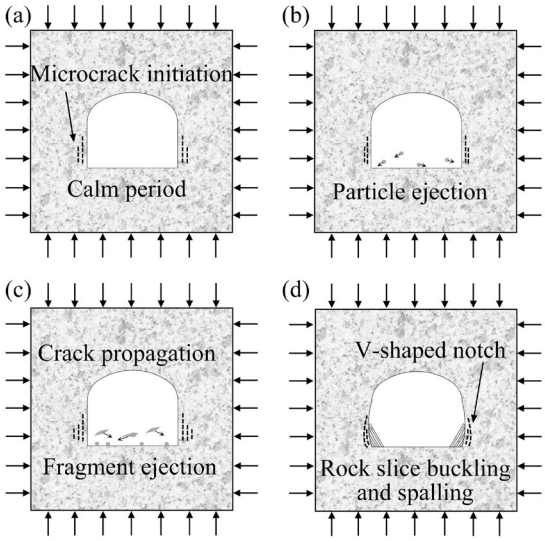

Fig. 10 Evolution process of sidewall failure under lower axial stresses of 10−60 MPa: (a) Calm stage; (b) Particle ejection stage; (c) Fragment ejection stage; (d) Rock slice buckling and spalling stage

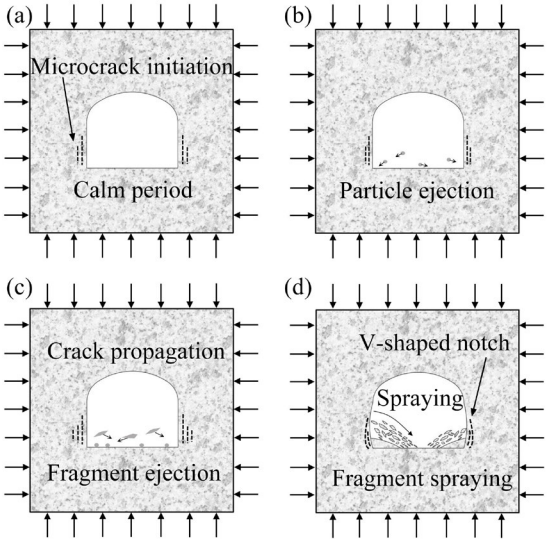

Fig. 11 Evolution process of sidewall failure under higher axial stresses of 70−80 MPa: (a) Calm stage; (b) Particle ejection stage; (c) Fragment ejection stage; (d) Fragment spraying stage

increases, the macroscopic cracks gradually expand and connect along the sidewall. The rock slice gradually buckles to the free surface and eventually peels off from the sidewalls. This stage is shown schematically in Fig. 10(d). It can be observed from Fig. 6 that the buckling and spalling stage of rock slices is a slow process. During this period, particle ejection, fragment ejection, and rock slice buckling and spalling occur continuously at other locations on both sidewalls, with obvious spatial distribution characteristics.

When the axial stress is high (70−80 MPa), the failure process of the sidewall can also be divided into four stages: the calm stage, the particle ejection stage, the fragment ejection stage, and the fragment spraying stage. As shown in Fig. 11, the failure characteristics of sidewalls at the first three stages are basically the same as those at the low axial stresses. However, the final failure stage, i.e., fragment spraying stage, is more violent compared with the rock slice buckling and spalling stage. As the vertical stress increases, a large number of rock particles and fragments are suddenly ejected from the sidewalls (Fig. 11(d)), creating a white fog phenomenon.

Table 1 shows the average durations at the four failure stages under different axial stresses. It can be observed that there is little difference in the duration of the calm stage under different axial stresses. At higher axial stresses (70−80 MPa), the duration of the particle ejection stage is shorter and the duration of the fragment ejection stage is obviously longer. This suggests that at higher axial stresses, the effect of non- uniformity caused by rock particles is weakened and more failure occurs in the form of fragment ejection from the sidewalls. In the last stage, the failure of the surrounding rock at lower axial stresses (10−60 MPa) is characterized by slow spalling failure of longer duration. In contrast, at higher axial stresses (70−80 MPa), due to the accumulation of more releasable elastic strain energy, the later failure stages of the surrounding rock are intensified, which is manifested as the longer duration for fragment ejection and the violent spraying of rock fragments. It can be concluded that axial stress has a significant impact on the failure evolution process of the surrounding rock. A higher axial stress shortens the duration of the particle ejection stage and lengthens the duration of the fragment ejection stage, and the suddenness of the rockburst is stronger.

Table 1 Durations at four failure stages under different axial stresses

Axial stress/ MPa	Duration/s			
	Calm stage	Particle ejection stage	Fragment ejection stage	Last stage
10−60	936.72	76.48	130.43	297.60
70−80	955.62	65.70	250.92	66.60

4.2 Influence of axial stress on failure stress

The initial vertical failure stress σ_{zi} in the surrounding rock under different axial stress conditions is shown in Fig. 12. As the axial stress increases, σ_{zi} increases first and then decreases. The σ_{zi} is the lowest when the axial stress is 10 MPa, and is the highest when the axial stress is 60 MPa. Hence, the stability of the surrounding rock is highest at an axial stress of 60 MPa. In previous studies, scholars tried to explain the causes of rock stability from different perspectives. For example, SU et al [20] introduced the constraint and Poisson effects to explain the variations in rock strength with increasing tunnel axial stress. DU et al [36] suggested that a high deviatoric stress between σ_2 and σ_3 causes more prominent pre-fracturing. Therefore, when σ_2 was increased to a certain value, the rock strength decreased. PAN et al [37] demonstrated that the number of rock failure elements in the pre-peak region is the decisive factor for the change in rock strength using the EPCA3D system numerical simulation method. Increasing σ_2 inhibits the deformation of the rock element in the vertical direction and delays rock failure. Hence, the rock strength increases. However, when σ_2 is sufficiently large, it leads to the failure of many rock elements, and thus causes a reduction in the rock strength.

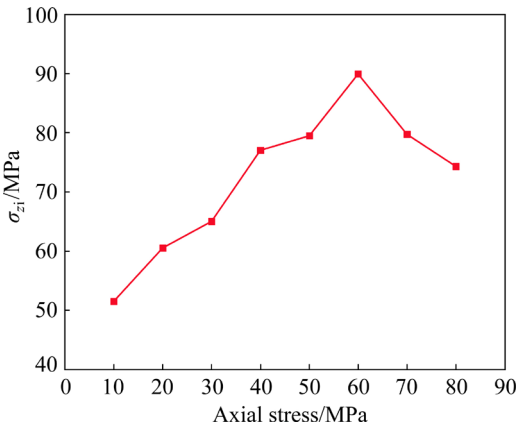

Fig. 12 Variation in σ_{zi} under different axial stress conditions

In fact, several cracks are randomly created in the surrounding rock before it starts to fail. The rock will fail if these cracks connect and penetrate. Here, we investigated the influence of axial stress on the rock strength using a microscopic view of the tiny rock element of the sidewalls, as shown in Fig. 13. For ease of understanding, three cracks A, B, and C are considered to represent the class of cracks in approximately parallel radial, axial, and vertical directions, respectively. An increase in axial stress (σ_2) promotes the closure of classes A and C cracks, resulting in an increase in the frictional resistance to inhibit their extension. Therefore, the strength of the surrounding rock increases. However, when the axial stress increases to 70 MPa, it has a limited effect on the closure of classes A and C cracks. The increase in axial stress will instead promote the expansion of class B cracks, making them easier to join and penetrate each other, thus reducing the overall strength of the surrounding rock.

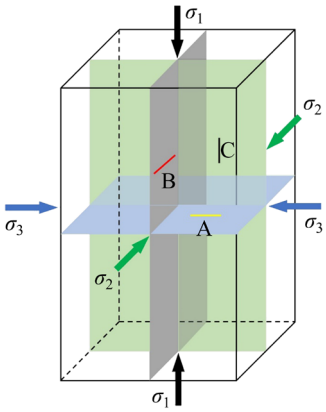

Fig. 13 Schematic diagram for rock element crack analysis

In order to further understand the stability of the surrounding rock in deep roadway under different axial stresses from a macroscopic point of view, the fragments of specimens were cleaned after the tests. The rock fragments were carefully clipped out with tweezers to ensure the integrity of the rock fragments. The overall failure of the specimens after cleaning is shown in Fig. 14. The final failure modes and areas of the surrounding rock are similar under different axial stress conditions. Failure starts on both sidewalls and progresses axially, forming a V-shaped notch. Moreover, when the axial stress is 10−40 MPa or 80 MPa, the macroscopic cracks connecting the hole and specimen boundary are produced. However, when the axial stress is 50−70 MPa, there are no macroscopic cracks in the whole specimen, indicating that low and high axial stresses are detrimental to the overall stability of the surrounding rock. An appropriate increase in axial stress can help to reduce crack generation and expansion. Therefore, excavating the roadway along the larger axial stress direction is recommended in practical engineering.

4.3 Influence of axial stress on failure intensity

Rock failure is a process driven by energy storage and release [38,39]. By comparing the sidewall failure evolution process under different axial stress conditions, it can be found that all the stored elastic strain energy is used for crack initiation and propagation under low vertical stress. When the cracks extend to the sidewall surface, the elastic strain energy is released in the form of particle ejection and fragment ejection. As the vertical stress continues to increase, once the outer rock fragments peel off and break to the free surface, the inner rock fragments are successively ejected. This phenomenon is particularly evident when high axial loads are applied. Under high axial stress conditions, the buckling time of the rock slices is very short, and they are all ejected from the sidewall at high speeds. Therefore, it can be concluded that a high axial stress level increases the intensity of the surrounding rock failure.

The slope of the cumulative AE count curve can effectively reflect the intensity of rock failure. The cumulative AE counts increase slowly during the initial and continuous loading phases. After entering the step loading stage, the cumulative AE counts increase rapidly. From Figs. 6 and 7, it can be observed that the violent rock failure occurs mainly in the last two stages. Therefore, the slope of the cumulative AE count curve is calculated by taking the micro time unit (0.1 s) in the last two loading stages, and then the average value of them is calculated. The average value of the slope of the cumulative AE count curve is shown in Table 2. As can be seen from Table 2, the curve of the cumulative AE counts roughly tends to become steeper as the axial stress increases. When the axial stress is 10−40 MPa, the AE activity distribution in the step loading stage is more uniform (as shown in Figs. 9(a−d)). However, at high axial stresses (50−80 MPa), the AE activity is mainly distributed in the last two loading stages (Figs. 9(e−g)), suggesting that high axial stress retards the fracture evolution process. The rock failure intensity is related to the elastic strain energy stored before rock failure. Although high axial stresses retard the failure evolution process, they provide a higher lateral constraint force, allowing the rock to store more elastic strain energy before failure. In this case, when the rock starts to fail, the stored elastic strain energy is released quickly, increasing the rock failure intensity.

According to the analysis above, it should be noted that a certain increase in axial stress can improve the overall stability of the surrounding rock. However, if the axial stress is too high, it can lead to intenser rock failure and significant hazards. Therefore, when choosing the axial direction of the roadway, the problem of increased failure intensity caused by high axial stress should also be considered.

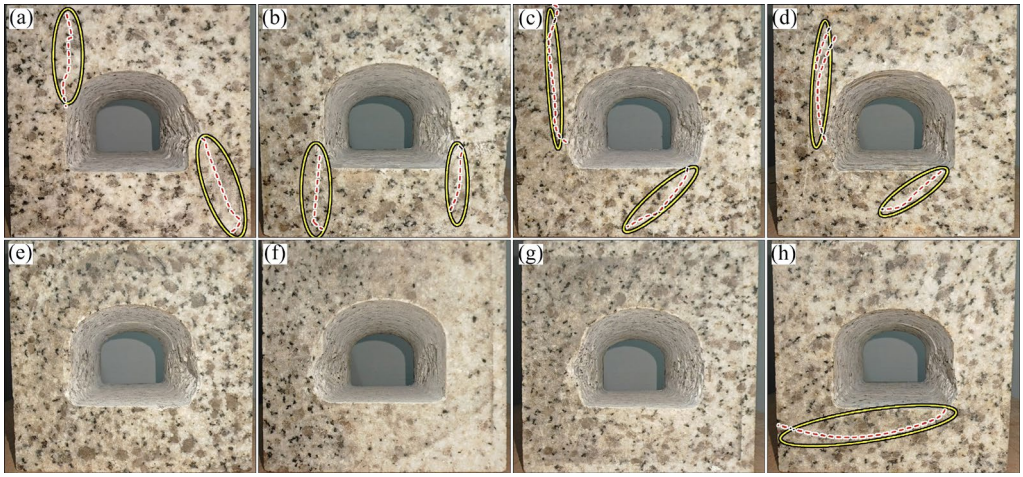

Fig. 14 Overall failure photographs of different specimens after fragment cleaning: (a) T-10-10; (b) T-10-20; (c) T-10-30; (d) T-10-40; (e) T-10-50; (f) T-10-60; (g) T-10-70; (h) T-10-80

Table 2 Average slopes of cumulative AE count curves

Axial stress/MPa	10	20	30	40	50	60	70	80
Average slope/10^4	0.62	3.04	3.38	3.44	4.32	3.50	3.52	5.92

4.4 Boundary effect via comparative tests

The boundary effect is desired to be considered in the true triaxial compression experiment on specimens containing holes. In general, the boundary width of the specimen needs to be 3−5 times (or more) the radius of the hole [40]. In our above work, the side length of the granite cube specimen is 100 mm. If the boundary width of the specimen is at least 5 times the radius of the hole, the radius will be less than 10 mm, making it difficult to observe the failure process of the surrounding rock of the hole. Therefore, we selected small hole specimens with a radius of approximately 12.5 mm (3 times) to conduct the comparative tests under seven axial stresses (10, 20, 30, 40, 50, 60, and 70 MPa) and to analyze the boundary effect. The dimensions of the rock specimens used for comparative tests are shown in Fig. 15. To differentiate from the above work, the rock specimens were also named according to the test type and preset values of the radial stress and axial stress. Namely, in the naming convention for the specimens, the first letter represents the comparative test and the second and third numbers represent the radial and axial stresses, respectively (i.e., C-10-10, C-10-20, C-10-30, C-10-40, C-10-50, C-10-60, and C-10-70). We controlled all specimens with the same stepped load path after reaching the initial stress state. That is, the force in the *Z*-direction is loaded in steps from 700 kN (20 kN per step and maintained for 1 min) and unloaded after maintaining for 1 min at 1100 kN.

Figure 16 shows the variations in σ_{zi} of the specimens containing 25 and 50 mm holes under different axial stresses. The initial vertical failure stress of 25 mm hole specimens under different axial stresses is 80, 86, 90, 88, 94.26, 72.65, and 70.01 MPa for Specimens C-10-10, C-10-20, C-10-30, C-10-40, C-10-50, C-10-60, and C-10-70, respectively. In other words, as the axial stress increases, the initial vertical failure stress first increases and then decreases. This finding is consistent with the variation law of the initial vertical failure stress observed in the true triaxial compression tests on 50 mm hole specimens. This indicates that although the boundary has an effect on the specific failure stresses under different axial stresses, it does not influence their variation laws.

Figure 17 shows the final failure of the surrounding rock of the 25 mm hole specimens under different axial stress conditions. No obvious V-shaped failure features are observed as the rock debris is not cleaned. However, careful observation reveals that the severest failure occurs in the middle of the sidewalls, similar to a V-shaped failure state. Moreover, as the axial stress increases, the failure degree of the surrounding rock decreases first and then increases, and only a small amount of rock buckling and spalling occurs in Specimen C-10-50. This indicates that the overall stability of the surrounding rock is the best under medium axial stress. This observation is also consistent with that obtained in the true triaxial compression experiments on the 50 mm hole specimens.

The comparative observations of the small-hole specimens show that the failure of the surrounding rock also proceeds in four stages: the calm stage, the particle ejection stage, the fragment ejection stage, and the rock slice buckling and spalling stage. The small hole specimen (C-10-30) is used as an example to illustrate the failure process of the surrounding rock. As shown in Fig. 18(b), at 1796.40 s and σ_z=90.00 MPa, particle ejection occurs at the left sidewall. After 24.84 s,

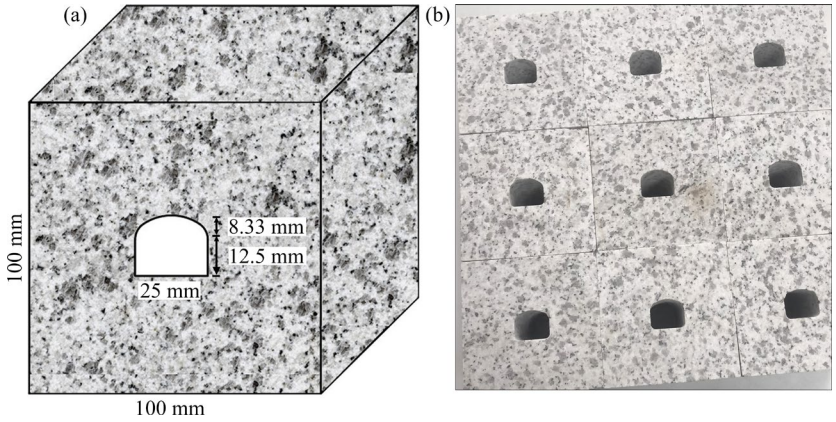

Fig. 15 Granite specimen (25 mm): (a) Sketch; (b) Physical photograph

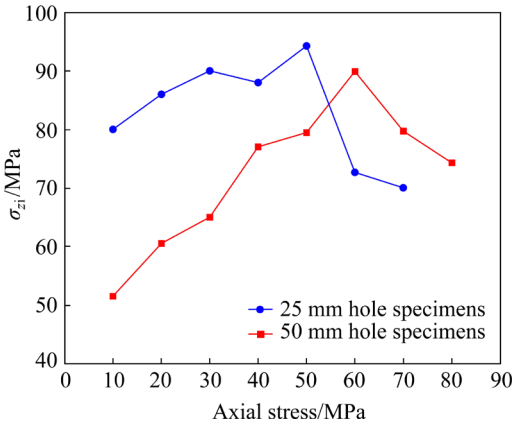

Fig. 16 Variations in σ_{zi} of specimens containing 25 and 50 mm holes

the right sidewall rock block suddenly peels off and is ejected along with several particles (Fig. 18(c)). At 1886.40 s and σ_z=92.00 MPa, fragments are ejected from the left sidewall (Fig. 18(d)). After about 71.64 s, another rock block is ejected from the left sidewall (Fig. 18(e)), and the failure gradually develops in the axial direction. At 2039.04 s and σ_z=96.00 MPa, the left sidewall rock slice buckles (Fig. 18(f)) and is spalled off after about 221.04 s (Fig. 18(g)). At 2345.04 s and σ_z= 103.34 MPa, the right sidewall rock slice begins to buckle (Fig. 18(h)). In the subsequent 319.04 s, the left sidewall failure gradually develops axially, spalling several rock slices (Fig. 18(j)). As shown in Fig. 18(k), a strong rockburst suddenly occurs in the surrounding rock, and several fragments are ejected, resulting in a white fog phenomenon. The final failure state of the surrounding rock is shown in Fig. 18(l).

Based on the above observations, we can infer that, when the hole size is small, the failure laws of 25 mm hole specimens observed under different axial stress conditions are consistent with those of the 50 mm hole specimens, indicating a limited boundary effect in the tests. Of course, we admit that the boundary has a significant impact on the deformation and failure of rock specimens with holes. For example, in this test, the overall strength of the specimens increased significantly when the hole size was small. This is mainly due to the increased boundary distance, which leads to a more difficult microcrack extension. However, HE et al [41] carried out true triaxial compression tests on 110 mm × 110 mm × 110 mm sandstone specimens with *d*50 mm circular holes, and obtained the failure characteristics of circular holes. LUO et al [42] studied the influence of water on the stress-induced failure of D-shaped hard rock tunnels by simulating rockburst experiments on red sandstone samples (100 mm × 100 mm × 100 mm) with D-shaped holes. The ratio of specimen size to hole size used in the above studies is 2.2 and 2.0, respectively. Although the influence of boundary effects exists, the failure of the chamber is better simulated and some meaningful conclusions are further drawn. WU et al [40] also compared the failure process of marble specimens (100 mm × 100 mm × 100 mm) containing holes of different sizes (40 mm × 40 mm and 25 mm × 25 mm) and discussed the boundary effects. They believed that larger hole specimens provided a better view of the hole failure process. In this study, we also adopted a similar experimental idea and discussed the

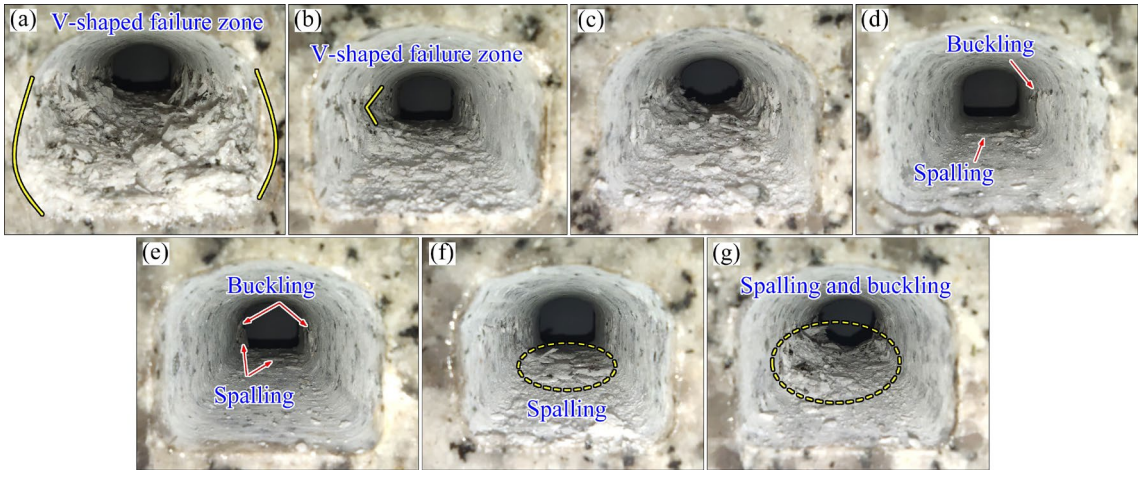

Fig. 17 Final failure images of surrounding rock for 25 mm hole specimens under different axial stress conditions: (a) C-10-10; (b) C-10-20; (c) C-10-30; (d) C-10-40; (e) C-10-50; (f) C-10-60; (g) C-10-70

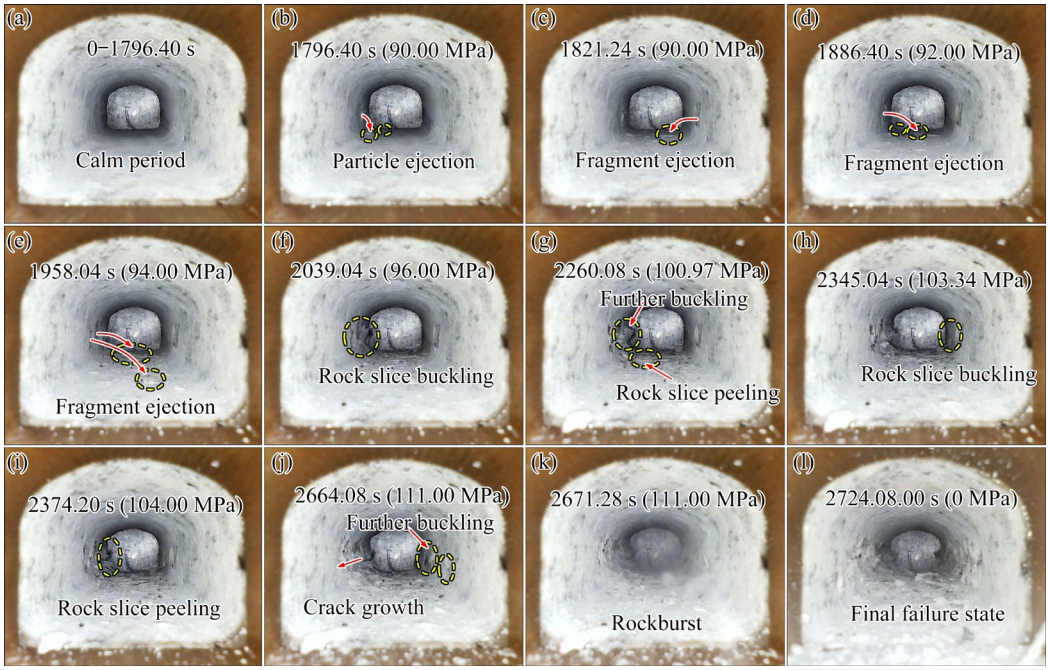

Fig. 18 Surrounding rock failure process images of 25 mm hole specimen (C-10-30)

boundary effect using comparative experimental results in a wider campaign (various axial stress conditions were simulated).

In summary, the failure characteristics and process of sidewalls observed in the small hole specimens are basically consistent with those in the large hole specimens. Although the boundary affects the overall strength of the specimens, it does not affect our major findings regarding the influence of axial stress on failure characteristics in arched roadways. Therefore, this study can help understand the failure characteristics of the roadway in underground engineering, which can guide the support and choice of excavation direction for roadways. In the future, further research can be carried out using large-size specimens under the condition of satisfying a large-scale true triaxial testing machine.

5 Conclusions

(1) Under low axial stresses, the failure process of surrounding rock can be divided into four stages: the calm stage, the particle ejection stage, the fragment ejection stage, and the rock slice buckling and spalling stage. Under high axial stresses, the failure process of surrounding rock includes the calm stage, the particle ejection stage, the fragment ejection stage, and the fragment spraying stage.

(2) As the axial stress increases, the initial vertical failure stress first increases and then decreases. This indicates that it is more difficult for initial failure to occur in the surrounding rock at moderate axial stress level.

(3) The failure intensity of the surrounding rock increases with increasing the axial stress. Therefore, the increased hazard contributed by higher axial stress should be considered when selecting the axial direction of the roadway.

(4) The failure characteristics and process of hole sidewalls observed in the small-hole specimens essentially match those in the large-hole specimens. Although the boundary effect affects the overall strength of the specimens, it does not affect our main findings regarding the influence of axial stress on the failure characteristics in arched roadways.

CRediT authorship contribution statement

Kang PENG: Investigation, Supervision, Funding acquisition, Project administration; **Ren-zhi LAI:** Investigation, Data curation, Formal analysis, Writing − Original draft; **Song LUO:** Investigation, Conceptualization, Methodology, Writing − Review & editing; **Xi-bing LI:** Investigation, Supervision.

Declaration of competing interest

The authors declare that they have no known competing financial interests or personal relationships

that could have appeared to influence the work reported in this paper.

Acknowledgments

This study was supported by the National Key Research and Development Program of China – 2023 Key Special Project (No. 2023YFC2907400), the Hunan Provincial Natural Science Foundation for Distinguished Young Scholars, China (No. 2023JJ10072), the Science and Technology Innovation Program of Hunan Province, China (No. 2022RC1173), and the Fundamental Research Funds for the Central Universities of Central South University, China (No. 2023ZZTS0499).

References

[1] KENETI A, SAINSBURY B A. Review of published rockburst events and their contributing factors [J]. Engineering Geology, 2018, 246: 361−373.

[2] LUO Song, GONG Feng-qiang, LI Liu-liu, PENG Kang. Linear energy storage and dissipation laws and damage evolution characteristics of rock under triaxial cyclic compression with different confining pressures [J]. Transactions of Nonferrous Metals Society of China, 2023, 33: 2168−2182.

[3] FENG Guang-liang, FENG Xia-ting, CHEN Bing-rui, XIAO Ya-xun, ZHAO Zhou-neng. Effects of structural planes on the microseismicity associated with rockburst development processes in deep tunnels of the Jinping. II: Hydropower Station, China [J]. Tunnelling and Underground Space Technology, 2019, 84: 273−280.

[4] FENG Guang-liang, FENG Xia-ting, CHEN Bing-rui, XIAO Ya-xun, YU Yang. A microseismic method for dynamic warning of rockburst development [J]. Rock Mechanics and Rock Engineering, 2015, 48: 2061−2076.

[5] FENG Xia-ting, LIU Jian-po, CHEN Bing-rui, XIAO Ya-xun, FENG Guang-liang, ZHANG Feng-peng. Monitoring, warning, and control of rockburst in deep metal mines [J]. Engineering, 2017, 3: 538−545.

[6] QIU Jia-dong, XIE He-ping, ZHU Jian-bo, WANG Jun, DENG Jian-hui. Dynamic response and rockburst characteristics of underground cavern with unexposed joint [J]. International Journal of Rock Mechanics and Mining Sciences, 2023, 169: 105442.

[7] LI Peng, CAI Mei-feng. Challenges and new insights for exploitation of deep underground metal mineral resources [J]. Transactions of Nonferrous Metals Society of China, 2021, 31: 3478−3505.

[8] XIAO Ying-ming, HE Man-chao, QIAO Ya-fei, PENG Meng-long, LI Hong-ru, CHENG Tai. A novel semi-analytical solution to ground reactions of deeply buried tunnels considering the nonlinear behavior of rocks [J]. Computers and Geotechnics, 2023, 159: 105429.

[9] BRUNING T, KARAKUS M, AKDAG S, NGUYEN G D, GOODCHILD D. Influence of deviatoric stress on rockburst occurrence: An experimental study [J]. International Journal of Mining Science and Technology, 2018, 28: 763−766.

[10] AMANN F, BUTTON E A, EVANS K F, GISCHIG V S, BLUMEL M. Experimental study of the brittle behavior of clay shale in rapid unconfined compression [J]. Rock Mechanics and Rock Engineering, 2011, 44: 415−430.

[11] SINGH S P. Classification of mine workings according to their rockburst proneness [J]. Mining Science and Technology, 1989, 8: 253−262.

[12] GONG Feng-qiang, YAN Jing-yi, LI Xi-bing, LUO Song. A peak-strength strain energy storage index for rock burst proneness of rock materials [J]. International Journal of Rock Mechanics and Mining Sciences, 2019, 117: 76−89.

[13] SU You-qiang, GONG Feng-qiang, LUO Song, LIU Zhi-xiang. Experimental study on energy storage and dissipation characteristics of granite under two-dimensional compression with constant confining pressure [J]. Journal of Central South University, 2021, 28: 848−865.

[14] ZHANG Wei, GUO Wei-yao, WANG Zhi-qi. Influence of lateral pressure on mechanical behavior of different rock types under biaxial compression [J]. Journal of Central South University, 2022, 29: 3695−3705.

[15] BAGDE M N, PETROS V. Fatigue properties of intact sandstone samples subjected to dynamic uniaxial cyclical loading [J]. International Journal of Rock Mechanics and Mining Sciences, 2005, 42: 237−250.

[16] HU Li-hua, YU Li-yuan, JU Ming-he, LI Xiao-zhao, TANG Chun-an. Effects of intermediate stress on deep rock strainbursts under true triaxial stresses [J]. Journal of Rock Mechanics and Geotechnical Engineering, 2023, 15: 659−682.

[17] CAI Ming. Influence of intermediate principal stress on rock fracturing and strength near excavation boundaries: Insight from numerical modeling [J]. International Journal of Rock Mechanics and Mining Sciences, 2008, 45: 763−772.

[18] LI Xi-bing, GONG Feng-qiang, TAO Ming, DONG Long-jun, DU Kun, MA Chun-de, ZHOU Zi-long, YIN Tu-bing. Failure mechanism and coupled static-dynamic loading theory in deep hard rock mining: A review [J]. Journal of Rock Mechanics and Geotechnical Engineering, 2017, 9: 767−782.

[19] LI Xi-bing, FENG Fan, LI Di-yuan, DU Kun, RANJITH P G, ROSTAMI J. Failure characteristics of granite influenced by sample height-to-width ratios and intermediate principal stress under true-triaxial unloading conditions [J]. Rock Mechanics and Rock Engineering, 2018, 51: 1321−1345.

[20] SU Guo-shao, JIANG Jian-qing, ZHAI Shao-bin, ZHANG Gang-liang. Influence of tunnel axis stress on strainburst: An experimental study [J]. Rock Mechanics and Rock Engineering, 2017, 50: 1551−1567.

[21] JIANG Bang-you, GU Shi-tan, WANG Lian-guo, ZHANG Guang-chao, LI Wen-shuai. Strainburst process of marble in tunnel-excavation-induced stress path considering intermediate principal stress [J]. Journal of Central South University, 2019, 26: 984−999.

[22] CHEON D S, JEON S, PARK C, SONG W K, PARK E S. Characterization of brittle failure using physical model experiments under polyaxial stress conditions [J]. International Journal of Rock Mechanics and Mining Sciences, 2011, 48: 152−160.

[23] LUO Song, GONG Feng-qiang. Evaluation of energy storage and release potentials of highly stressed rock pillar from rockburst control perspectives [J]. International Journal of Rock Mechanics and Mining Sciences, 2023, 163: 105324.

[24] KABWE E, KARAKUS M, CHANDA E K. Proposed solution for the ground reaction of non-circular tunnels in an elastic-perfectly plastic rock mass [J]. Computers and Geotechnics, 2020, 119: 103354.

[25] LIU Chong-yan, ZHAO Guang-ming, XU Wen-song, MENG Xiang-rui, HUANG shun-jie, ZHOU Jun, WANG Yun-kun. Experimental investigation on failure process and spatio-temporal evolution of rockburst in granite with a prefabricated circular hole [J]. Journal of Central South University, 2020, 27: 2930−2944.
[26] WANG Yang, LING Kai, YANG Yuan-yuan, ZHANG Zi-qian, XING Si-qi, HE Man-chao, LIU Dong-qiao. Experimental study on rockburst of surrounding rock in an elliptical tunnel with different axial ratios [J]. Tunnelling and Underground Space Technology, 2023, 140: 105329.
[27] HU Xiao-chuan, SU Guo-shao, CHEN Guan-yan, MEI Shi-ming, FENG Xia-ting, MEI Guo-xiong, HUANG Xiao-hua. Experiment on rockburst process of borehole and its acoustic emission characteristics [J]. Rock Mechanics and Rock Engineering, 2019, 52: 783−802.
[28] YANG Bei-bei, HE Ming-ming, XIAO Zhan-shan, ZHAO Jian-bin, ZHANG Yong-hao. Effect of horizontal stress on fractal characteristics of rockburst fragments in coal mining [J]. Energy, 2023, 281: 128181.
[29] GONG Feng-qiang, LUO Yong, LI Xi-bing, SI Xue-feng, TAO Ming. Experimental simulation investigation on rockburst induced by spalling failure in deep circular tunnels [J]. Tunnelling and Underground Space Technology, 2018, 81: 413−427.
[30] SI Xue-feng, HUANG Lin-qi, GONG Feng-qiang, LI Xi-bing. Failure process and characteristics of three-dimensional high-stress circular tunnel under saturated water content [J]. Transactions of Nonferrous Metals Society of China, 2022, 32: 2696−2708.
[31] SI Xue-feng, HUANG Lin-qi, GONG Feng-qiang, LIU Xi-ling, LI Xi-bing. Experimental investigation on influence of loading rate on rockburst in deep circular tunnel under true-triaxial stress condition [J]. Journal of Central South University, 2020, 27: 2914−2929.
[32] PENG Kang, YI Guan-sheng, WANG Yuan-min, LUO Song, WU Hao. Experimental and theoretical analysis of spalling in deep hard rock tunnels with different arch structures [J]. Theoretical and Applied Fracture Mechanics, 2023, 127: 104054.
[33] MUNOZ H, TAHERI A, CHANDA E K. Rock drilling performance evaluation by an energy dissipation based rock brittleness index [J]. Rock Mechanics and Rock Engineering, 2016, 49: 3343−3355.
[34] WANG J A, PARK H D. Comprehensive prediction of rockburst based on analysis of strain energy in rocks [J]. Tunnelling and Underground Space Technology, 2001, 16: 49−57.
[35] FENG Xia-ting, HAIMSON B, LI Xiao-chun, CHANG Chan-dong, MA Xiao-dong, ZHANG Xi-wei, INGRAHAM M, SUZUKI K. ISRM suggested method: Determining deformation and failure characteristics of rocks subjected to true triaxial compression [J]. Rock Mechanics and Rock Engineering, 2019, 52: 2011−2020.
[36] DU Kun, YANG Cheng-zhi, SU Rui, TAO Ming, WANG Shao-feng. Failure properties of cubic granite, marble, and sandstone specimens under true triaxial stress [J]. International Journal of Rock Mechanics and Mining Sciences, 2020, 130: 104309.
[37] PAN Peng-zhi, FENG Xia-ting, HUDSON J A. The influence of the intermediate principal stress on rock failure behaviour: A numerical study [J]. Engineering Geology, 2012, 124: 109−118.
[38] LUO Song, GONG Feng-qiang, PENG Kang, LIU Zhi-xiang, Influence of water on rockburst proneness of sandstone: Insights from relative and absolute energy storage [J]. Engineering Geology, 2023, 323: 107172.
[39] ZHANG Pei-lei, GONG Feng-qiang, LUO Song, SI Xue-feng, XU Lei. Damage constitutive model of uniaxially compressed coal material considering energy dissipation [J]. Journal of Materials Research and Technology, 2023, 27: 920−931.
[40] WU Wu-xing, GONG Feng-qiang, YANG Wei-min. Experimental simulation study of spalling in deep rectangular tunnel with plastic fine grain marble [J]. Tunnelling and Underground Space Technology, 2020, 98: 103319.
[41] HE Man-chao, XIA Hong-man, JIA Xue-na, GONG Wei-li, ZHAO Fei, LIANG Kang-yuan. Studies on classification, criteria and control of rockbursts [J]. Journal of Rock Mechanics and Geotechnical Engineering, 2012, 4: 97−114.
[42] LUO Yong, GONG Feng-qiang, ZHU Chuan-qi. Experimental investigation on stress-induced failure in D-shaped hard rock tunnel under water-bearing and true triaxial compression conditions [J]. Bulletin of Engineering Geology and the Environment, 2022, 81: 76.

轴向应力对深部硬岩拱形巷道破坏特性的影响

彭 康，赖仁志，罗 松，李夕兵

中南大学 资源与安全工程学院，长沙 410083

摘 要：为在考虑结构效应的基础上研究轴向应力对深部拱形巷道破坏特性的影响，对含贯穿三心拱型孔洞的立方体花岗岩试样进行真三轴压缩实验。实验过程中采用视频监控装置记录围岩破坏过程。实验结果表明，在10~60 MPa 的轴向应力条件下，围岩破坏经历了平静期、颗粒弹射、块片弹射及岩片屈曲和剥落 4 个阶段。在较高轴向应力(70 和 80 MPa)条件下，围岩破坏的第 4 阶段中出现了剧烈块片喷射现象。随着轴向应力的增大，围岩破坏剧烈程度增大，但初始破坏竖向应力先增大后减小。基于不同轴向应力条件下巷道的破坏特征，建议巷道沿着中等水平轴向应力方向布置。

关键词：轴向应力；破坏特征；真三轴试验；拱形巷道；V 型槽；声发射；岩爆

(Edited by Wei-ping CHEN)